Photon bunching reveals single-electron cathodoluminescence excitation efficiency in InGaN quantum wells

Sophie Meuret,[1] Toon Coenen,[1,2] Hans Zeijlemaker,[1] Michael Latzel,[3,4] Silke Christiansen,[3] Sonia Conesa Boj,[5] and Albert Polman[1]

1. Transmission electron microscopy

In order to determine the sample geometry, a TEM cross section was made using focused-ion-beam (FIB) milling (FEI Nova Nanolab 600i DualBeam system). For this procedure, the sample was initially covered by a thin Pt layer to protect the sample during the milling. The specimen was then characterized using high-angle annular dark field scanning transmission electron microscopy (HAADF STEM). These measurements were performed in a FEI Titan cube operated at 300 kV. An image of the InGaN quantum wells embedded in the GaN matrix is shown in Fig. S1(a). The lighter stripes correspond to InGaN quantum wells and the darker regions to GaN, since the contrast is correlated with the In content (Z-contrast image). We also observe a dark stripe in the top of the image, corresponding to the AlGaN barrier layer. This was confirmed with chemical analysis shown in Fig. S1(b). Energy dispersive X-ray (EDX) measurements were carried out in the same microscope equipped using a EDX silicon drift detector (SDD). In Fig. S1(b) an EDX line profile is shown measured along the arrow in (a). The AlGaN and InGaN layers are clearly visible as peaks in the Al and In signals. The data verifies the presence of the QWs and the AlGaN barrier layer.
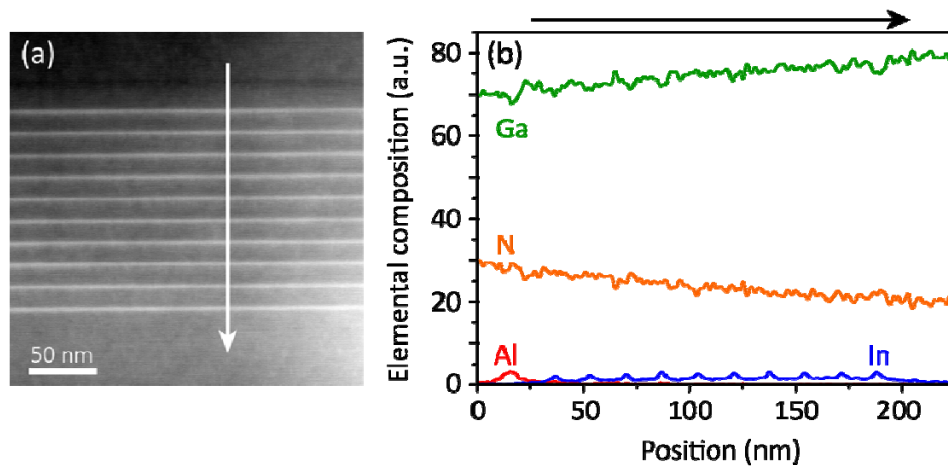

Figure S1: (a) HAADF STEM image of the InGaN/GaN sample cross section. **(b)** Chemical composition of the sample (in arbitrary units) as function of depth derived from the EDX data that was acquired along the white arrow in (a).

2. Detection setup and hardware

The CL was collected using a SPARC CL system (DELMIC BV) mounted on a Thermo Fisher/FEI Quanta FEG 650 scanning electron microscope. For the spectroscopy measurements we used a back-illuminated Newton DU940P BU2 CCD camera (2048 × 512 pixels). The camera was fully binned in the vertical direction while no horizontal binning was used in order to have the highest spectral resolution. We used a 300 lines/mm grating blazed for 500 nm wavelength mounted in a 193 mm Czerny-Turner spectrograph to obtain all relevant spectral contributions in a single acquisition. The entrance slit of the spectrometer was set to 100 µm which provides a good compromise between spectral resolution and efficient light incoupling. Achromatic lenses were used with VIS/NIR anti-reflection coatings which, together with the diffraction grating effectively, limit the systems response to the 360 – 1000 nm wavelength range.

For the $g^{(2)}$ measurements we coupled the CL into a 100 µm core VIS/NIR multimode fiber which was used to guide the light to the HBT experiment. After exiting the fiber the light is collimated and filtered with a short-pass color filter (< 500 nm). A neutral density filter was used to regulate the light intensity on the detectors to prevent damage. The light is detected using two single-photon avalanche diodes (SPADS) with a 100 x 100 μm^2 detection area (PicoQuant) connected to a PicoHarp 300 time-correlator unit (PicoQuant). These SPADS are able to detect light down to a wavelength of 400 nm and as a result we are effectively measuring a band from 400 – 500 nm. The SPADS are covered with IR filters to prevent cross talk between the detectors.

The SEM was blanked with a fast electrostatic blanker which was driven using homebuilt electronics. The blanking was triggered with an electrical pulse from a digital delay generator (Stanford Research Systems, DG645).

For every $g^{(2)}$ acquisition we optimized the optical alignment and measured the current before and after the experiment using a Faraday cup. Typical acquisition times were around 1000 s in continuous mode and around 3000 s in pulsed mode, and the acquisition was stopped when the noise in the lineshape was at an acceptable level. The histogram binning for the time correlator was set to 512 ps. For the angle-resolved measurement shown in section 3 the light was directed towards a Zyla sCMOS camera (2560 × 2160 pixels). The angular patterns were collected at full resolution (no binning).

3. Spectral data acquisition, system correction, and data analysis

We obtained spectra at the same acceleration voltages as for the photon correlation measurements. For every voltage we readjusted the current and checked the optical alignment of the system. Because of the large changes in light yield for different voltage, different dwell times were used to prevent clipping of the signal. The beam current was adjusted to be approximately the same for all measurements using a Faraday cup. We checked whether the current remained stable by remeasuring the current again after each experiment.

Energy (keV)	6	7	8	9	10	15	20	25	30
Current (pA)	10.5	10.7	10.6	10.5	10.5	10.4	10.2	10.2	10.3
T (ms)	500	500	500	500	400	250	250	400	500

Table 1: Measured beam current and used dwell time for different electron energies.

At every acceleration voltage setting we acquired CL data in an electron scan area of 10 × 10 pixels (70 nm step size). For every integration time a corresponding dark measurement was taken where the electron beam was blanked. To correct for the system response we measured the transition

radiation (TR) signal from a Czochralski-grown single-crystal aluminium substrate. In this case we took a scan of 8 × 8 pixels and 20 s integration time at 1.37 nA to obtain a smooth spectrum with low noise. For both the GaN and Al measurements we divide by the number of electrons (I*T/e) such that we obtain spectra in units of cts/electron. To check the consistency, we also measured spectra on the Al with 10, 1, and 0.5 s which yielded a very similar system response albeit with increasingly more noise.

By dividing by a theoretically calculated TR spectrum [1] [2] we can accurately determine the system response. As input for the calculation we use a dielectric function measured with ellipsometry on the same sample. Transition radiation has a toroidal angular radiation pattern which is different from the QW emission pattern and this can be taken along in the system response correction. The emission pattern for the QW is measured using angle-resolved CL imaging [3]. Figure S2(a) shows an angular pattern averaged over 16 patterns collected in a 4 × 4 grid (1 μm pixel size). The measurement was performed using an electron energy of 10 keV, a beam current of 20 pA, and a 10 s dwell time. No color filter was used as the CL is fully dominated by the QW emission at this electron energy. The observed pattern is Lambertian similar to what we observed earlier for bulk GaAs [2]. The close similarity with a Lambertian profile is also apparent in the angular cross cut shown in Fig. S2(b).
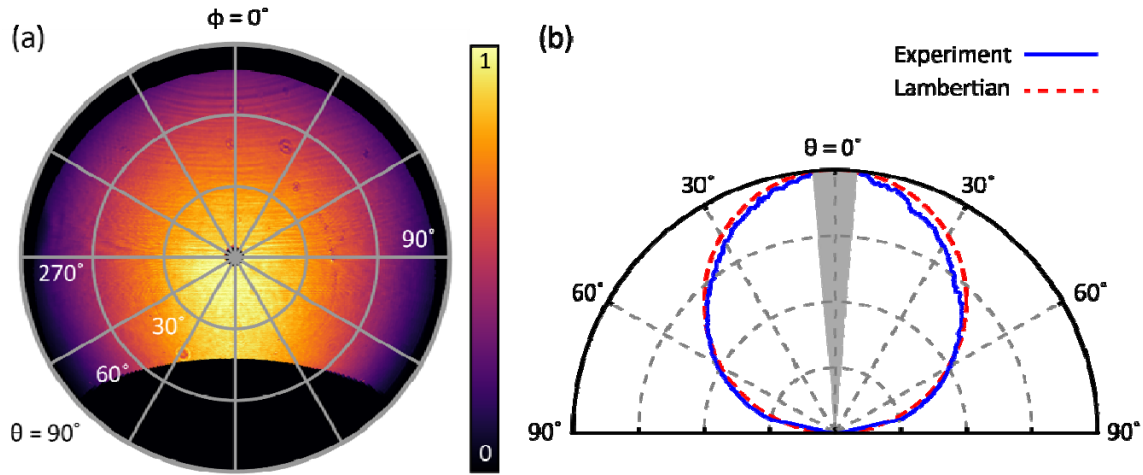

Figure S2: (a) Angular pattern showing CL intensity as function of zenithal angle θ and azimuthal angle φ for the InGaN QW well emission. **(b)** Angular cross cut through data in (a). The data was integrated from φ = 270 - 0 and from 0° - 90° for the left and right half of the curve. The gray wedge indicated part of the pattern that is not collected due to the hole in the mirror. For reference we show a theoretical Lambertian curve (red dashed line).

The Lambertian emission is directed more towards the normal than the toroidal TR emission. Because the mirror geometry and corresponding acceptance angle are known we can calculate the collection efficiency difference between the transition radiation and the Lambertian InGaN emission from which we find 83 and 86% respectively; this effect it is taken into account in the system correction analysis. The system response corrects for the wavelength dependent response of the optical detection system (parabolic mirror, vacuum window, lenses, incoupling, grating, and camera). We note that the polarization also plays a role in the collection efficiency but this is neglected because it is only a small effect [4] [5]. Because we use a back-thinned CCD camera there is some effect of etaloning in the spectra beyond λ = 650 nm which is also (partly) corrected for by the system response (see Fig. S3 (a),(c)). Spectra acquired in the wavelength domain are converted to the energy domain using the appropriate Jacobian conversion factor $(hc)/(\lambda^2 e)$.
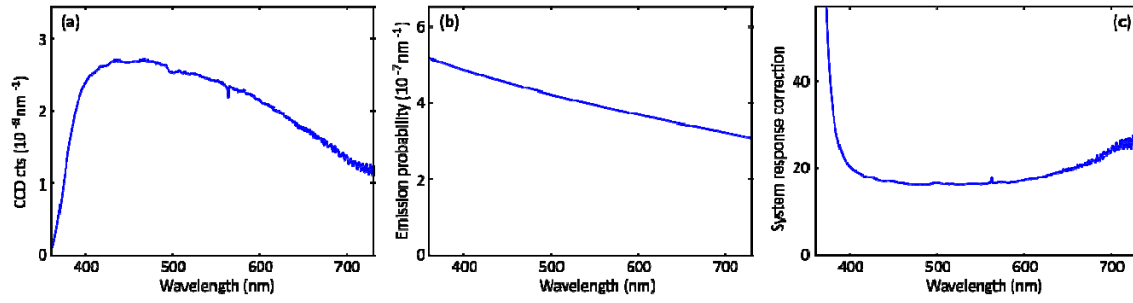
Figure S3: (a) Raw CL spectrum measured on single-crystal Al in units of CCD cts per pixel per incident primary electron. **(b)** Theoretical calculation of the TR emission probability. **(c)** System response correction defined as the ratio between the curves in (b) and (a).

In our experimental geometry a large portion of the light emitted by the quantum wells remains trapped within the material due to total internal reflection at the GaN/vacuum interface. Nevertheless, we can estimate how much light is generated inside the material by calculating the outcoupling efficiency of light generated through an electron-hole recombination event. For this estimate, we calculate the outcoupling efficiency of a point dipole placed in bulk GaN at a given depth below the GaN/vacuum interface. This is done for dipoles either parallel and normal to the interface. The full Green's tensor is taken into account [6] and tabulated values are used for the refractive index of GaN [7]. The outcoupling for the out-of-plane dipole orientation is very low (0.48% for the quantum well emission a depth of 335 nm) because the majority of the light is emitted sideways beyond the critical angle (24.6 degrees for n = 2.4), whereas for the in-plane dipole a significant portion is emitted within the critical angle (4.8%). Taking into account the measured Lambertian angular profile in Fig. S2 we assume the emission to be isotropic, *i.e.* there is no preferred dipole orientation for recombination within the quantum well. Figure S4(a) shows the outcoupling efficiency as a function of depth and emission energy assuming an isotropically averaged dipole orientation. The oscillatory behavior is caused by variation in the local optical density of states, well-known from Drexhage [8]. Figure S4 (b) shows the outcoupling efficiency averaged over the QW depths. At 2.77 eV the efficiency is 3.5%; this value is used to scale the data in Fig. 1(f).
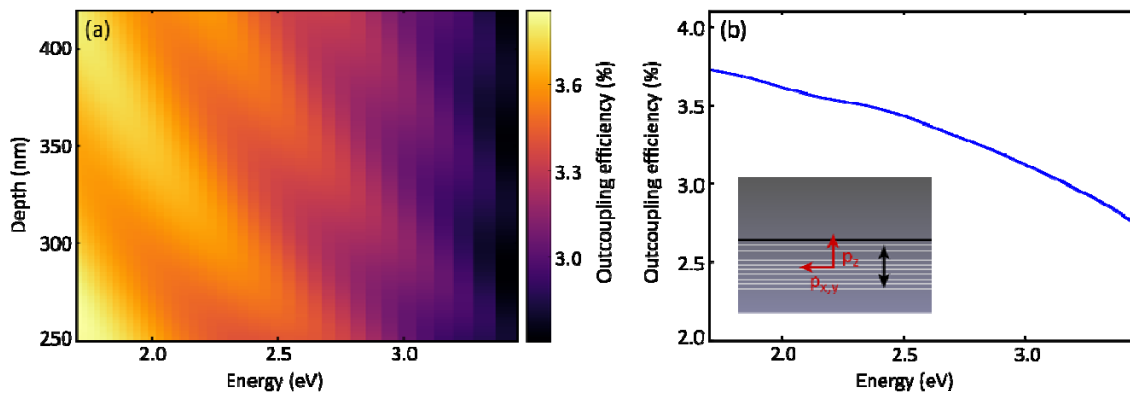

Figure S4: (a) Outcoupling efficiency as a function of photon energies and wavelength assuming an isotropically-averaged dipole orientation. **(b)** Outcoupling efficiency as function of photon energy averaged over the dipole orientation and depth range corresponding to the quantum wells.

4. Numerical fitting of the spectral CL data

The CL spectra are fitted in the energy domain, using data corrected for the system response as described in section 3. We find that the yellow band (YB) emission is well-approximated by a Gaussian, line shape while the GaN and InGaN emission peaks are better approximated with a combined Lorentzian/Gaussian line shape where the relative ratio is an additional fit-parameter. The fitting was performed using a least-squares fitting routine. We restrict the peak energies and widths to values close to those found at 30 keV (see Fig. S5 (a)) to prevent unphysical results, particularly for low peak amplitudes as is the case for the YB and GaN band gap below 15 keV. From the fits it follows that the peak positions and widths do not significantly vary for different voltages. The QW peak is slightly asymmetric which we attribute to the discrete nature of the QWs (small changes in size/composition can slightly shift the QW emission wavelength). The band gap emission possibly is not fully resolved as it is right at the edge of the spectral detection range which could also lead to a small non-physical asymmetry in the peak-shape as well. The edge of the detection range in the UV is mainly determined by the grating and the achromatic VIS/NIR coated lenses in the CL detection system.
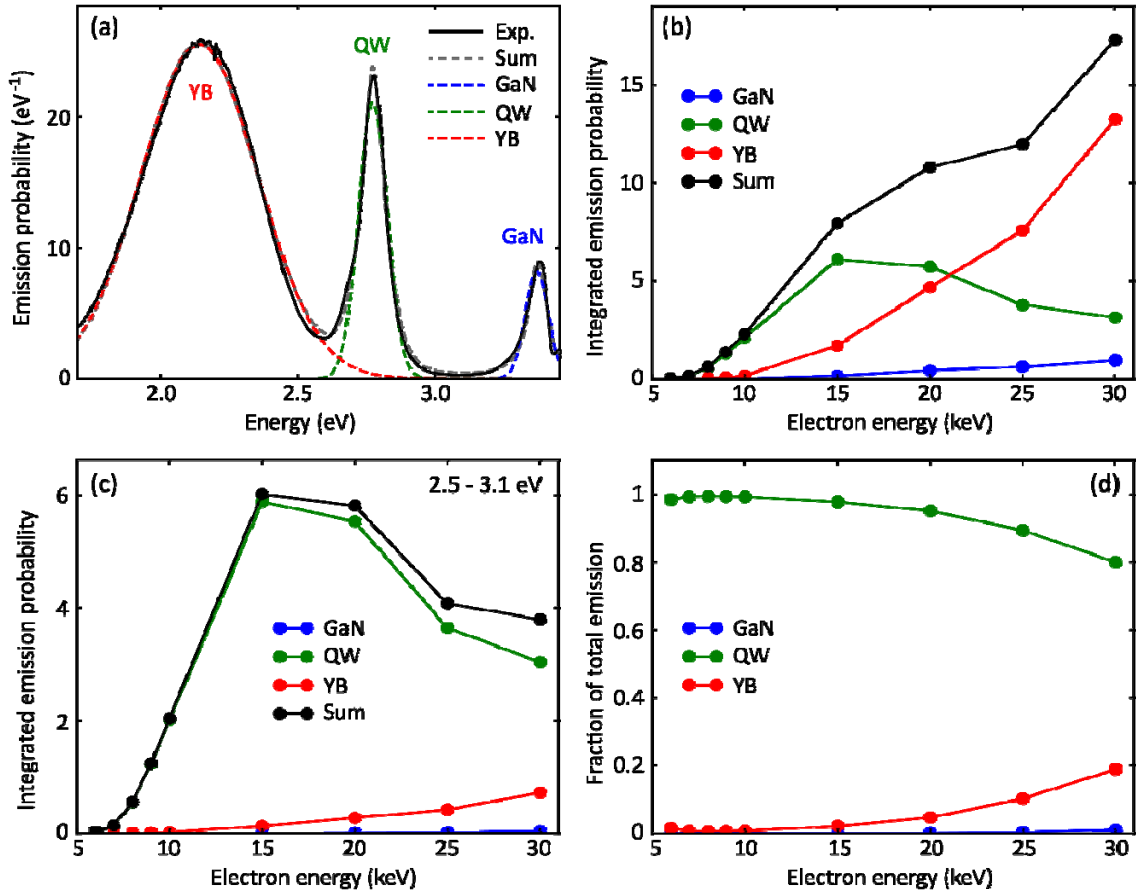

Figure S5: (a) Experimental CL spectrum measured at 30 keV (solid curve) shown together with the total fit and the three separate fitted peaks (dashed curves). **(b)** The individual fitted peaks are integrated to yield a total emission probability for the different contributions in the spectrum (GaN,

QW, and YB). **(c)** Total emission probability of the different CL peaks within the filter window (2.5 – 3.1 eV). **(d)** Fraction of total emission for the different CL peaks within the filter window.

Emission peak	Peak position (eV)	FWHM (eV)
GaN	3.37	0.08
QW	2.77	0.10
YB	2.14	0.50

Table 2: Peak positions and FWHM for the GaN, QW, and YB spectral features as extracted from the fits.

The fitted peak positions and line widths and full-width half-maximum (FWHM) are listed in Table 2. The fitting procedure allows us to estimate the contribution of the bandgap, YB, and QW emission as function of acceleration voltage integrated over the full spectral range (Fig. S5(b)), as well as within the filter range used for the $g^{(2)}$ experiment (Fig. S5(c)). To obtain the internal emission probability we correct for the outcoupling efficiency as was also done in Fig. 1(f). Figure S5(b) shows that the overall emission probability increases with voltage and that the YB becomes the dominant CL emission peak for higher voltages. Within the filter range the QW emission remains dominant; above 15 keV its emission decreases due to the reduced overlap of the electron cloud with the QW. The relative YB contribution increases in the filter range for higher voltages (see Fig. S5 (d)) which has a small effect on the shape of the $g^{(2)}$ curve because the YB has longer radiative lifetime.

5. $g^{(2)}$ simulation and analysis
Normalization of the $g^{(2)}$ in pulsed and continuous mode

To normalize $g^{(2)}$ we consider that the number of counts at large delay (> 300 ns for continuous and 1000 ns for pulsed excitation) represents the uncorrelated events and therefore should reflect the Poissonian distribution of electrons in the continuous electron beam produced by the tip. In a Poissonian source, electrons are randomly distributed in time. Therefore N_{tot}, the number of events recorded during a time T for delays between τ and $\tau + \Delta t$, is equal to $TN_1N_2\Delta t$ where N_1 and N_2 are the number of counts per second recorded on the two detectors. We can verify the Poissonian character of the electron distributions as follows. Figure S7 shows one of the $g^{(2)}$ measurement of Fig. 2 before normalization. For this acquisition $N_1 = N_2 = 5 \times 10^4$ cts/s, T = 700 s and Δt = 512 ps and hence N_{tot} = 896, which is shown as a dashed red line in Fig. S7. It is clear that the number of counts at large delay in the CL data matches the behavior of a Poissonian beam. Note that the same normalization procedure is also used in $g^{(2)}$ measurement using laser excitation.

In pulsed mode the behavior of the source is unchanged, as the pulse generation is performed after the emission of electrons from the source by electrostatically chopping the beam. The Poissonian distribution is therefore maintained inside the pulse and the second peak which physically represents the correlation of photons produced by two consecutive pulses can also be considered Poissonian and as such can be normalized to unity, again similar to the convention in a pulsed laser beam experiments.
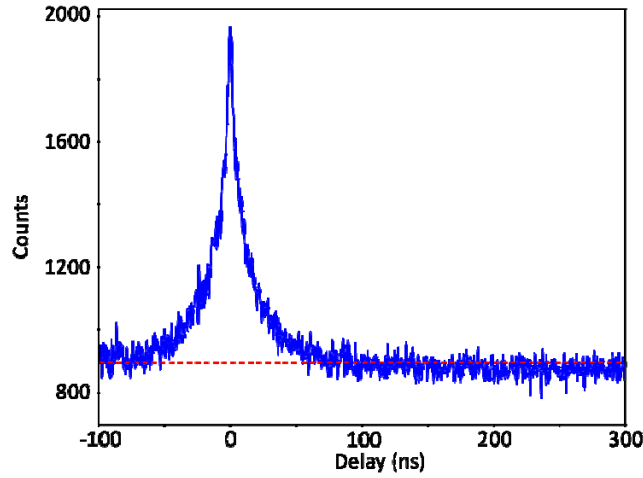
Figure S6 : $g^{(2)}$ measurement (blue line) for an electron beam current I = 20 pA. The red line shows the number of counts expected for a continuous Poissonian beam at the same acquisition conditions ($N = 5 \times 10^4$, T = 700 s and Δt = 512 ps). At large delay the behavior observed is consistent with a Poissonian electron source.

Lifetime of CL emission

The CL lifetime can be extracted using two different methods, either by doing an exponential fit of the $g^{(2)}$ function or acquiring a decay trace using a pulsed excitation as described in section 5. In the microscope both methods are available. Figure S8 shows the resulting fit for the two methods at 10 keV. We find that the $g^{(2)}$ function is best fitted with a double exponential decay of τ_1 = 12 and τ_2 = 35 ns. To verify the origin of these decay times we also acquired decay traces at the QW wavelength (< 500 nm) and at the YB wavelength (510 - 590 nm). Figure S8(b) shows the result for the QW emission. Because the decay is very fast we fit an exponential convoluted with a Gaussian (250 ps FWHM). We find a decay time of 11.5 ns, close to τ_1 in (a). This single-exponential fit seems to fit the data rather well. Figure S8(c) shows the result for the YB wavelength. Clearly, the decay is significantly slower than the QW emission. We find that this is fitted best with a double exponential decay. In this case the faster component (τ_{YB1}) is close to τ_2. The slower component τ_{YB2} is not visible in the $g^{(2)}$ curve because it is obscured in the background.
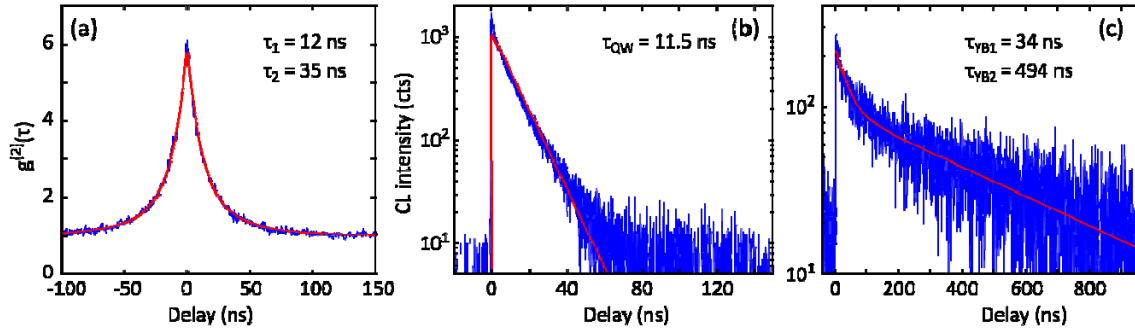
.

Figure S7 : **(a)** $g^{(2)}$ measurement at 10 keV (blue line) and corresponding fit (red line). The retrieved lifetimes are in the figure. In the fit τ_1 is representing 80% of the signal **(b)** Decay trace measured for the QW wavelength with a histogram binning of 64 ps. **(c)** Decay trace measured at the YB

wavelength with a histogram binning of 512 ps. Because of the longer decay times the exact lifetime that is retrieved is quite sensitive to the choice of background level. We estimate the resulting errors to be ± 5 ns for τ_{YB1} and ± 50 ns for τ_{YB2}.

Isolation of the fitted component in the $g^{(2)}$ equation

If the emission decay is the result of two distinct emission sources, with two different lifetimes the resulting radiative decay is described by a double exponential and the amplitude of $g^{(2)}$ at $\tau = 0$ will be the result of both emission sources. As explained in the main text the $g^{(2)}(\tau)$ function is fitted by double-exponential line shapes:

$$g_{tot}^{(2)}(\tau) = 1 + g_{QW}^{(2)}(0)exp\left(-\frac{|\tau|}{\tau_{QW}}\right) + g_{YB}^{(2)}(0)exp\left(-\frac{|\tau|}{\tau_{YB}}\right)$$

In order to compare the Monte Carlo model that only takes into account the interaction with the QWs and the CL experiments in which both QW and YB emission contribute, it is important to understand the influence of the YB emission on the resulting $g^{(2)}$ amplitude at $\tau = 0$. If two uncorrelated signals S and B, with respective lifetimes τ_{QW} and τ_{YB} are considered, the $g^{(2)}_{tot}(\tau)$ function can be written as :

$$
\begin{aligned}
g_{tot}^{(2)}(\tau) &= \frac{\langle\left(S(t)B(t)\right)\left(S(t+\tau)B(t+\tau)\right)\rangle}{\langle S(t)+B(t)\rangle^2} \\
&= \frac{\langle S(t)S(t+\tau)\rangle}{\langle S(t)\rangle^2}\frac{\langle S(t)\rangle^2}{\langle S(t)+B(t)\rangle^2} + \frac{\langle B(t)B(t+\tau)\rangle}{\langle B(t)\rangle^2}\frac{\langle B(t)\rangle^2}{\langle S(t)+B(t)\rangle^2} \\
&= g_S^{(2)}(\tau)\rho^2 + g_B^{(2)}(\tau)(1-\rho^2) \\
&= \left(1+g_S^{(2)}(0)\,exp\left(-\frac{\tau}{\tau_{QW}}\right)\right)\rho^2 + \left(1+g_B^{(2)}(0)exp\left(-\frac{\tau}{\tau_{YB}}\right)\right)(1-\rho^2) \\
g_{tot}^{(2)}(\tau) &= 1 + \underbrace{\rho^2 g_S^{(2)}(0)}_{g_{QW}^{(2)}}\,exp\left(-\frac{\tau}{\tau_{QW}}\right) + (1-\rho^2)g_B^{(2)}(0)\,exp\left(-\frac{\tau}{\tau_{YB}}\right)
\end{aligned}
$$

where the signal to background ratio ρ is defined as $S/(S+B)$. Therefore the amplitude of the $g^{(2)}$ in case where only the quantum wells are excited corresponds to :

$$g_S^{(2)}(\tau) = \frac{g_{QW}^{(2)}(\tau)}{\rho^2}$$

We can see here that if ρ is decreasing the amplitude at $\tau = 0$ is increasing which corresponds to a reduced interaction in the bunching model.

At 10 keV, $\rho = 0.88$ and therefore, because it is close to one, the amplitude of the fit component at $\tau = 0$ can be used as a the actual amplitude of the $g^{(2)}_{QW}(0)$. Using the amplitude of the fit of the short decay component is a small correction. Even without this correction a good agreement between the Monte Carlo simulation and the experimental data is found as shown in Figure S9 where the total amplitude at $\tau = 0$ from the experimental data is plotted. This validates the approach used in the main text.
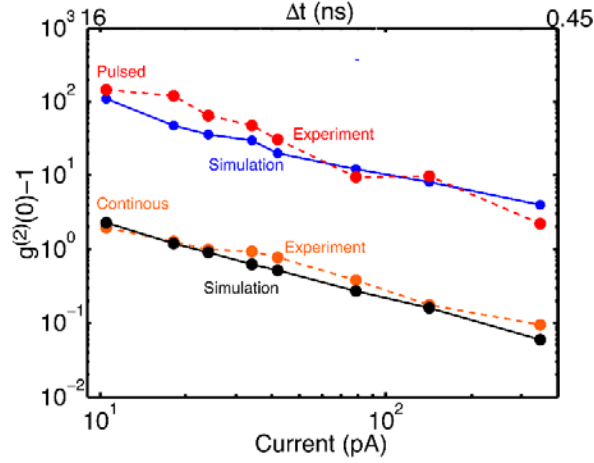
Figure S8: Same figure as Fig. 4(b) of the main text but here the total amplitude of the $g^{(2)}$ at τ = 0 has been taken into account.

Definition of γ

In the model used to simulate the $g^{(2)}$ for electron excitation (as reported in Fig. 4), one of the important parameters that will influence the value of $g^{(2)}(0)$ is γ, the fraction of electrons that interact with the quantum wells. We take the following steps for the $g^{(2)}$ Monte Carlo simulations:

1: At $t = t_1$ the incoming electron creates N bulk plasmons ($E_{plasmon}$ = 20 eV) [10] that will excite the quantum wells. This number N is determined by a Poissonian distribution centered around the efficiency of excitation γ_e:

$$P_N = \frac{1}{N!}\gamma_e{}^N \exp\left(-\gamma_e\right)$$

2: The N plasmons decay in 2 electron-hole pairs [11] that can excite the quantum wells with a quantum efficiency of η.

3: For each electron-hole pair excitation the quantum well decays through emission of a photon, at a time $t = t_2$ determined by the radiative probability P_{rad}

$$P_{rad}(t_2) = \frac{1}{\tau_1}\exp\left(-\frac{t_2 - t_1}{\tau_1}\right)$$

In the model it can be shown that the number of electron hole pairs generated per plasmon does notg significantly influence the $g^{(2)}$ curve (see Figure S10), and η has no influence either. On the other hand, γ_e and as well as the current I and the lifetime τ_1 do strongly affect the result. From γ_e we can retrieve the fraction of electrons that create bulk plasmons (γ) and resulting electron-hole pairs that interact with the quantum wells ($N > 0$).
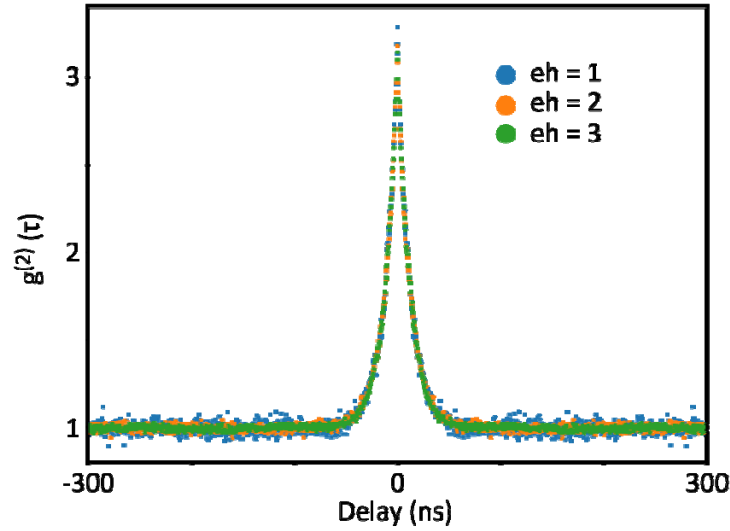
Figure S9: Monte Carlo simulation of the $g^{(2)}$ for $\gamma = 0.5$, $\tau_{QW} = 12$ ns and $I = 10.5$ pA, and the number of eh pairs per bulk plasmon of 1 (blue dots), 2 (orange dots) and 3 (green dots). The results are almost identical.

6. Pulse width characterization

The pulse width was characterized using transition radiation (TR) from a single-crystal gold substrate. In this case all the collected light was guided to one SPAD only. The signal from this SPAD was then correlated with the triggering signal from the delay generator which allows to directly measure the CL signal decay with respect to the incoming electron pulse. Normally this method can be used to extract the lifetime of the CL emission. As the lifetime of the TR is negligibly short compared to the pulse duration (< 30 fs) [9] the measured signal fully reflects the shape of the electron pulses.
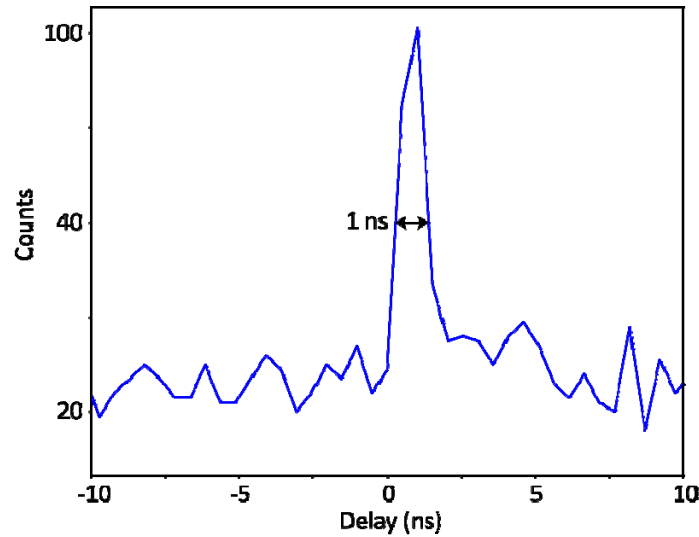

Figure S10: Pulse width characterization at 10 keV. The time histogram was binned at 512 ps. The pulse full width at half maximum is shown (1 ns).

Figure S6 shows the measurement of the pulse shape at 10 keV.. Because the TR signal at 10 keV is low the binning of the histogram in the time correlator was set to 512 ps to improve the signal to noise ratio, thereby limiting the resolution of the measurement. The full width at half maximum

found is 1 ns; Because transition radiation is rather inefficient at 10 keV we used the highest continuous current available (around 10 nA), far from the low current used for the $g^{(2)}$ measurement of Fig 4 (10.5 pA). It is known that the time resolution of beam blanking improves for lower current; therefore the measurement shown in Figure S6 presents an upper limit of the pulse duration. For the simulation, we assume a pulse duration of 0.5 ns, which leads to good fits of the model; the fit results are not very sensitive to the pulse duration.

7. Casino simulations and diffusion model

The diffusion model uses Casino simulations that simulate the trajectory of electrons inside the material [12].
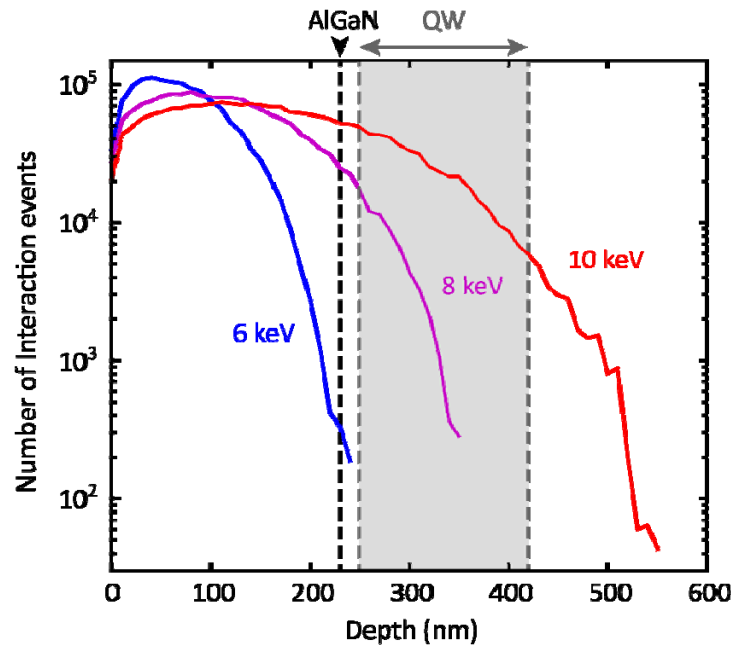

Figure S11: Distribution of electron interactions (2400 electron trajectories simulated) as function of depth, binned in 10 nm depth bins for 6, 8, and 10 keV primary electron energy. The position of the AlGaN barrier layer and QW region are indicated by the dashed lines.

For each incoming electron simulated by Casino, the depth Z_e of each interaction is extracted as shown in Fig. S11 for 6, 8, and 10 keV. Depending on where the excitation is created the probability P_{ex} for the electron hole pairs created to reach the quantum wells is equal to:

    i.   If $Z_e < L_{AlN}$: $P_{ex} = 0$

    ii.   If $L_{AlN} < Z_e < L_{QW1}$:   —

    iii.   If $L_{QW1} < Z_e < L_{QW2}$: $P_{ex} = 1$

    iv.   If $Z_e > L_{QW2}$:   —

With D_{L1} and D_{L2} the diffusion length respectively before and after the quantum well (in Fig. S12 the relevant parameters are indicated). As $L_{AlN} = L_{QW1}$-30 (nm) D_{L1} does not have a significant influence on the results. D_{L2} on the other hand will have an influence for high voltage where most of the excitations are generated beyond the quantum well region ($Z_e > L_{QW2}$). As D_{L2} is the relevant diffusion parameter we refer to it as D_L in the paper.
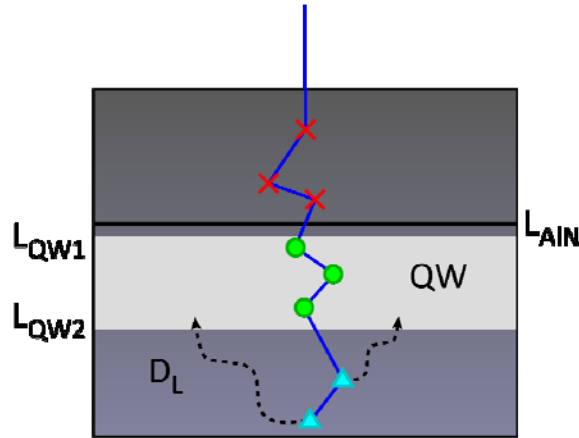

Figure S12: Sketch showing the relevant parameters for the diffusion model.

[1] F. J. García de Abajo, "Optical Excitation in Electron Microscopy," *Rev Mod Phys,* vol. 82, p. 209, 2010.

[2] B. J. M. Brenny, T. Coenen and A. Polman, "Quantifying coherent and incoherent cathodoluminescence in semiconductors and metals," *Journal of Applied Physics,* vol. 115, p. 244307, 2014.

[3] T. Coenen, E. J. R. Vesseur and A. Polman, "Angle-resolved cathodoluminescence imaging spectroscopy," *Appl. Phys. Lett.,* vol. 99, p. 143103, 2011.

[4] T. Coenen and A. Polman, "Polarization-sensitive cathodoluminescence Fourier microscopy," *Opt. Express,* vol. 20, p. 18679, 2012.

[5] C. I. Osorio, T. Coenen, B. J. M. Brenny, A. Polman and A. F. Koenderink, "Angle-resolved cathodoluminescence imaging polarimetry," *ACS Photonics,* vol. 3, p. 147, 2016.

[6] J. Sipe, "New Green-function formalism for surface optics," *J. Opt. Soc. Am. B,* vol. 4, pp. 481-489, 1987.

[7] A. J. Barker and M. Llegems, "Infrared Lattice Vibrations and Free-Electron Dispersion in GaN," *Phys. Rev. B.,* vol. 7, pp. 743-750, 1973.

[8] K. Drexhage, "Influence of a dielectric interface on fluorescence decay time," *J. Lumin.,* Vols. 1-2, p. 693, 1970.

[9] B. J. M. Brenny, A. Polman and F. J. García de Abajo, "Femtosecond plasmon and photon wave packets excited by a high energy electron on a metal or dielectric interface," *Phys. Rev. B,* vol.

94, p. 155412, 2016.

[10] X. Kong, A. Bengoechea-Encabo, M. Sanchez-Garcia, E. Calleja and A. Trampert, "Plasmon excitation in electron energy-loss spectroscopy for determination of indium concentration in (In,Ga)N/GaN nanowires," *Nanotechnology,* vol. 23, p. 485701, 2012.

[11] A. Rothwarf, "Plasmon theory of electron-hole pair production: efficiency of cathode ray phosphors," *Journal of Applied Physics,* vol. 44, no. 2, p. 752, 1973.

[12] H. Demers, N. Poirier-Demers, A. Réal Couture, D. Joly, M. Guilman, N. De Jonge and D. Drouin, "Three-Dimensional Electron Microscopy Simulation with the Casino Monte Carlo Software," *Scanning,* vol. 33, pp. 135-146, 2011.